Optimization of heterogeneous continuous flow hydrogenation using FTIR inline analysis: a comparative study of multi-objective Bayesian optimization and kinetic modeling

Kejie Chai [a], Weida Xia [a], Runqiu Shen [a], Guihua Luo [a], Yingying Cheng [a], Weike Su [a, *], An Su [b, *]

[a] *Key Laboratory of Pharmaceutical Engineering of Zhejiang Province, National Engineering Research Center for Process Development of Active Pharmaceutical Ingredients, Collaborative Innovation Center of Yangtze River Delta Region Green Pharmaceuticals, Zhejiang University of Technology, Hangzhou, 310014, P. R. China*

[b] *College of Chemical Engineering, Zhejiang University of Technology, Hangzhou 310014, P. R. China*

Corresponding Authors:

Prof. An Su
College of Chemical Engineering, Zhejiang University of Technology, Hangzhou 310014, P. R. China
Email: ansu@zjut.edu.cn

Prof. Weike Su
Key Laboratory of Pharmaceutical Engineering of Zhejiang Province, National Engineering Research Center for Process Development of Active Pharmaceutical Ingredients, Collaborative Innovation Center of Yangtze River Delta Region Green Pharmaceuticals, Zhejiang University of Technology, Hangzhou, 310014, P. R. China
Email: pharmlab@zjut.edu.cn

Graphical Abstract

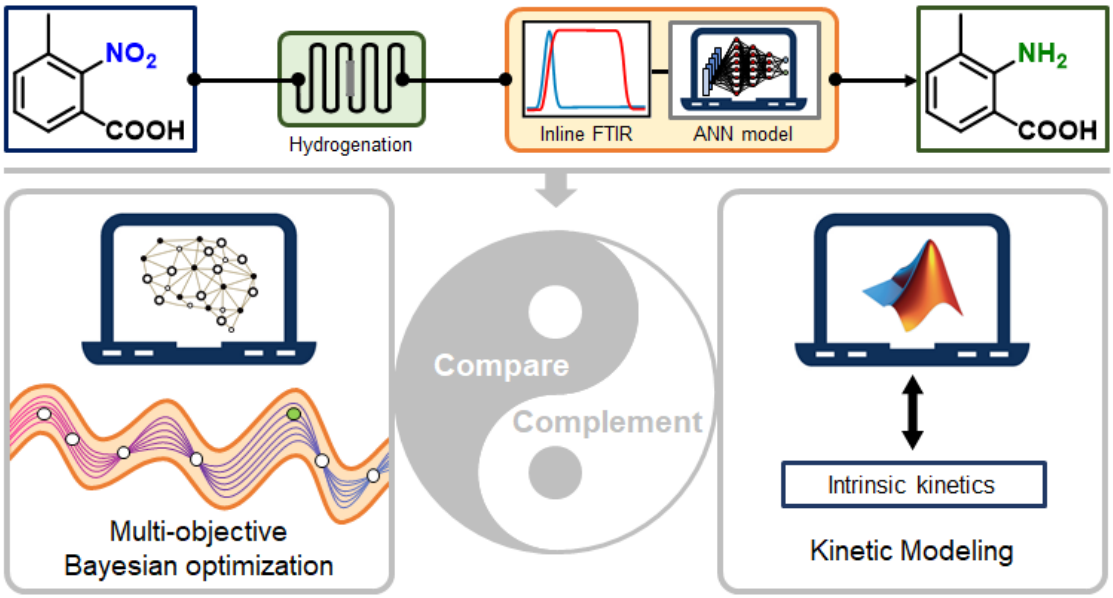

Abstract

The heterogeneous continuous flow hydrogenation is pivotal in chemical research and production, yet its reaction optimization has historically been intricate and labor-intensive. This study introduces a heterogeneous continuous flow hydrogenation system specifically designed for the preparation of 2-amino-3-methylbenzoic acid (AMA), employing FTIR inline analysis coupled with an artificial neural network model for monitoring. We explored two distinct reaction optimization strategies: multi-objective Bayesian optimization (MOBO) and intrinsic kinetic modeling, executed in parallel to optimize the reaction conditions. Remarkably, the MOBO approach achieved an optimal AMA yield of 99% and a productivity of 0.64 g/hour within a limited number of iterations. Conversely, despite requiring extensive experimental data collection and equation fitting, the intrinsic kinetic modeling approach yielded a similar optimal AMA yield but a higher productivity of 1.13 g/hour, attributed to increased catalyst usage. Our findings indicate that while MOBO offers a more efficient route with fewer required experiments, kinetic modeling provides deeper insights into the reaction optimization landscape but is limited by its assumptions.

Keywords

Multi-objective Bayesian optimization; Kinetic modeling; continuous flow; heterogeneous hydrogenation; Reaction optimization; Inline analysis

Introduction

Heterogeneous catalytic hydrogenation is pivotal in organic synthetic chemistry, with broad applications across the dye, pharmaceutical, and fine chemical industries.[1-3] Traditional intermittent hydrogenation processes, however, are constrained by critical safety concerns associated with reaction temperature and pressure, prompting a shift towards continuous flow hydrogenation as a safer and more efficient alternative.[4, 5] The reaction optimization within these continuous flow systems has emerged as a research focus.[6, 7] Historically, the reaction optimization process predominantly employed the one factor at a time (OFAT) method [8], which relies on a sequential, factor-based optimization guided by chemical intuition[9-12]. Despite its widespread use, the OFAT approach is often criticized for its inefficiency and inaccuracy, primarily due to its inability to account for potential synergistic effects among various factors, potentially leading to misinterpretation of the chemical processes.[13] Consequently, there is a pressing need for developing systematic approaches to reaction optimization.

Kinetic modeling, grounded in a comprehensive understanding of chemical processes, represents a classical and crucial strategy for reaction optimization, especially for heterogeneous hydrogenation reactions.[14-17] For instance, Su et al. demonstrated the application of kinetic modeling in the heterogeneous flow hydrogenation of hexafluoroacetone trihydrate, revealing an adsorption-desorption mechanism with competitive adsorption of H_2 dissociation.[18] Similarly, Yu et al. conducted a continuous hydrogenation study of 2-(4-nitrophenyl) butanoic acid and kinetics study in a micropacked-bed reactor, employing kinetic analysis to elucidate the impacts of internal and external diffusion, as well as salt formation.[19] Despite these advances, the application of kinetic modeling in heterogeneous catalysis is often hampered by the complexities associated with non-chemical kinetics phenomena.[20-24]

Multi-objective Bayesian Optimization (MOBO) has revolutionized the optimization of continuous-flow reactions by adeptly handling competing objectives.[25-28] It

leverages the surrogate model and acquisition function to systematically explore the Pareto Front, aiming to strike an optimal balance among objectives. Using probabilistic models, MOBO predicts outcomes for specific reaction conditions, guiding the optimization process toward superior performance metrics. Recent significant implementations of MOBO include Jensen et al.'s optimization of multistep synthetic routes on an automated platform [25], Bourne et al.'s achievement of an 81% yield through the simultaneous optimization of telescoped reactions [29], and Lapkin et al.'s application of MOBO in medicinal chemistry for yield optimization [30]. Despite its advancements, MOBO's comparison with traditional optimization methods is less studied.

Inline analytical techniques, including inline FTIR, NMR, and UV/vis spectroscopy, are becoming integral to reaction optimization due to their ability to provide real-time data, which facilitates the creation of self-optimizing systems when combined with Bayesian optimization.[29, 31, 32] Kappe et al. have notably advanced this field by integrating four complementary inline analysis instruments and developing advanced data analysis models, which quantify desired products, intermediates, and impurities inline across various stages of a multi-step synthetic pathway.[33] Furthermore, they have successfully applied artificial neural networks (ANN) for processing NMR and UV/vis spectra of multiple components.[34] Besides enhancing Bayesian optimization, inline analysis is also anticipated to improve the efficiency of traditional optimization techniques, such as kinetic modeling.

In this study, we focused on the synthesis of 2-amino-3-methylbenzoic acid, a key intermediate for the pesticide chlorantraniliprole, to serve a case study for optimizing heterogeneous continuous flow hydrogenation. We designed a continuous flow hydrogenation system equipped with an FTIR for inline monitoring and analysis of reaction data. Multi-objective Bayesian optimization and kinetic modeling were conducted in parallel to optimization the reaction process, allowing us to compare the advantages and limitations of these two approaches directly.

Materials and Methods

Materials. 3-Methyl-2-nitrobenzoic acid (98%, MNA), 2-amino-3-methylbenzoic acid (98%, AMA), methanol (MeOH, analytical grade), and silica (100-200 mesh) were purchased from Sinopharm Chemical Reagent Co., Ltd. (SCRC) without further purification. Hydrogen (H_2, 99.999%) and nitrogen (N_2, 99.999%) were purchased from Hangzhou Jingong Special Gas Co., Ltd. The catalyst Pd@SBA-15 was synthesized following the method reported in our previous work.[35]

Experimental setup. Metering pump (JJRZ-10004F) was purchased from Hangzhou Jingjin Technology Co., Ltd. High performance liquid chromatography (HPLC) column (5 mm in diameter and 50 mm long) was purchased from Dalian Baijia Lida Technology Co., Ltd. Check valve, T-joint mixer, temperature sensor, pressure gauge, back pressure regulator, and stainless steel tube (1/8" and 1/16" outside diameter) were purchased from Beijing Xiongchuan Technology Co., Ltd. Polytetrafluoroethylene (PTFE) tube (1/8" and 1/16" outside diameter) was purchased from Nanjing Runze Fluid Control Equipment Co., Ltd. Inline FTIR (ReactIR 702L) was purchased from Mettler Toledo Technology Co., Ltd. Mass flow controller (D07) was purchased from Beijing Sevenstar Flow Co., Ltd. Water bath was purchased from Heidolph Instruments Co., Ltd. Experimental setup was shown in Figure S1a.

Heterogeneous continuous flow hydrogenation system. MNA was dissolved in MeOH and pumped into the continuous flow system through a metering pump. The flow rate and pressure of H_2 involved in the hydrogenation were controlled by adjusting the mass flow controller and the pressure gauge, respectively. The gas and liquid flow tubes were fitted with check valves to avoid backflow. The hydrogen and MNA solution were mixed in a T-joint mixer and then flowed into a 1.0-meter pretreatment tube to reach hydrogenation temperature. The synthesized catalyst Pd@SBA-15 was pre-loaded in an HPLC column and the remaining space was filled with silica. Then, sieve

plates were installed at the ends of the HPLC column as a micro pack-bed reactor (MPBR). The MPBR was placed vertically in a hot water bath, which facilitates full contact between the gas-liquid mixture and the catalyst. The gas-liquid mixture undergoes hydrogenation in the MPBR. The pressure of the entire system was controlled by a manual back pressure regulator. The water bath and temperature sensor accurately control the hydrogenation temperature together. The check valve and back pressure regulator ensured that the continuous flow system was isolated from air. Then, the gas-liquid mixture flowed into a 1.0-meter pretreatment tube in a cold water bath to reach 20 ˚C. Inline FTIR monitored the concentrations of MNA and AMA after the hydrogenation in real-time. The tubes for solution flow through the inline FTIR were PTFE tubes and all other tubes were stainless steel tubes. The entire heterogeneous continuous flow hydrogenation system was controlled by adjusting the reaction parameters, such as temperature, flow rate, and hydrogen pressure.

Concentration determination. Concentrations of MNA and AMA in the reaction solution were monitored in real-time by inline FTIR. ANN modeling was performed as a processing approach for inline FTIR spectra data according to the reported literature (Figure S2a).[34] Several groups of MNA and AMA in methanol solution with different concentrations were prepared and their inline FTIR spectra data were collected as training set and validation set. Here the verification set is equivalent to the test set (Table S1). Next, 5000 analog spectra are generated from a linear combination of two pure components, and Gaussian noise is added to augment the training set. Some of the data simulating the experimental process were also added to the training set and validation set. To improve the stability and performance of the ANN training phase, all spectra data were normalized. Next, during the training process, an architecture of one convolutional layer followed by dense layers was investigated. The spectra data was processed at the Conv1D convolutional layer for characteristic extraction to screen the weights of the data. Then, data dimension reduction was performed through different functions in the dense layers. Finally, the output layer outputs the predicted concentrations of MNA and AMA. Compared with the known concentration in the test

set, the predicted results of the model are basically consistent, indicating that the ANN model framework developed for this purpose is suitable (Figure S2b). The inline FTIR spectra data monitored during the experiment were used to quickly predict the concentrations of MNA and AMA through the ANN model. The conversion of the MNA ($\mathrm{Conversion_{MNA}}$), the yield of the AMA ($\mathrm{Yield_{AMA}}$), and the productivity of the AMA ($\mathrm{Productivity_{MNA}}$) in the continuous flow hydrogenation system were calculated through Equation 1, Equation 2, and Equation 3, respectively:

$$\mathrm{Conversion_{MNA}} = 1 - \frac{C_{\mathrm{MNA}}}{C^0_{\mathrm{MNA}}} \quad (1)$$

$$\mathrm{Yield_{AMA}} = \frac{C_{\mathrm{AMA}}}{C^0_{\mathrm{MNA}}} \quad (2)$$

$$\mathrm{Productivity_{MNA}} = C_{\mathrm{AMA}} F_{\mathrm{MNA}} M_{\mathrm{AMA}} \quad (3)$$

where C^0_{MNA} was the initial concentration of the MNA in the solution; C_{MNA} and C_{AMA} were the concentration of the MNA and the AMA in the collected solution, respectively; F_{MNA} was the flow rate of the MNA solution; M_{AMA} was the molar mass of the AMA.

Multi-objective Bayesian Optimization. MOBO was performed according to the following process in general.[36, 37] The Bayesian optimizer was initialized by the design of experiments (DoE) or the random collection of initial experimental condition parameters and results. The expectation and uncertainty of each point were predicted based on a probabilistic surrogate model generated from the initial experimental results, with the trade-off between exploration and exploitation of the response space. Among them, the exploration region had high uncertainty, while the exploitation focuses on the part with high predictive expectations. New experimental condition parameters were obtained to perform new experiments after maximizing the acquisition function. The experimental dataset was then extended and reused to train a more accurate surrogate model. This process was iterated until obtaining satisfactory reaction yield and productivity.

The initial sampling, the surrogate model, and the acquisition function as the three core

196 sections formed the MOBO model.[38, 39] Latin Hypercube Sampling (LHS) was used
197 as the initial sampling approach to avoid the presence of excessive data aggregation in
198 simple random sampling. The LHS divided the sampling units into different layers
199 according to some characterization or some rules, and then extracted samples
200 independently and randomly from the different layers. Notably, the LHS uses fewer
201 samples than the traditional OFAT or DoE approach when the same threshold is reached,
202 thus reducing the complexity of the calculation.
203
204 MOBO was a response surface approach to uncertainty guidance, in which the
205 performance of the surrogate model represented the predictive accuracy of the
206 optimizer.[36] The efficiency of the surrogate model could only be recognized if its
207 estimations of expectation and variance were close enough to the true response
208 surface.[36] Gaussian process (GP) was an infinite-dimensional extended function
209 distribution frequently used as the surrogate model.[39] GP allowed the construction of
210 joint probability distributions of variables for estimating the variance and mean of the
211 predicted data based on the available data. The Matérn class was a commonly used class
212 of covariance functions in GP, *via* Equation 4:[40]

213 $$M_{\text{Matérn}}(x,y) = \frac{2^{1-\nu}\sigma^2}{\Gamma(\nu)}\left(\sqrt{2\nu}\|x-y\|\right)^{\nu} K_{\nu}\left(\sqrt{2\nu}\|x-y\|\right) \quad (4)$$

214 Where $\sigma^2 > 0$ and $\nu > 0$; ν, σ^2, $\Gamma(\nu)$, $\|x-y\|$, and K_{ν} were the non-negative
215 parameter, the output variance, the gamma function, the distance between two points,
216 and the Bessel function, respectively.
217
218 Furthermore, the acquisition function was crucial for the desired optimization
219 performance. Among them, probabilistic improvement (PI), expected improvement
220 (EI), and upper confidence bound (UCB) are frequently used to tune hyperparameters.
221 The *q*-noisy expected hypervolume improvement (*q*NEHVI) function was superior to
222 other existing acquisition functions for MOBO, for example, it enabled one-step
223 hypervolume maximization in both noisy and noise-free environments, *via* Equation
224 5:[41, 42]

$$\alpha_{q\mathrm{NEHVI}}(\chi_{\mathrm{cand}}|\mathcal{P}) = \frac{1}{\widetilde{N}}\sum_{t=1}^{\widetilde{N}} \mathrm{HVI}\left(\tilde{f}_t(\chi_{\mathrm{cand}}|\mathcal{P})\right) \quad (5)$$

where $\widetilde{N}$, HVI, $\tilde{f}_t$, χ_{cand}, and $\mathcal{P}$ were the number of samples, the hypervolume improvement, the posterior sample, the candidate sample, and the Pareto boundary, respectively.

In this work, the *q*NEHVI function was used to optimize the yield of the AMA ($\mathrm{Yield_{AMA}}$) and the productivity of the AMA ($\mathrm{Productivity_{MNA}}$) in the continuous flow hydrogenation system.

Results and discussion

In this study, a continuous flow hydrogenation system (Figure 1) was constructed to perform the hydrogenation of MNA using an MPBR filled with Pd@SBA-15 catalyst. Real-time reaction monitoring was achieved through an inline FTIR instrument, the ReactIR 702L. The data collected via inline FTIR were processed using an ANN model, enabling the acquisition of real-time concentration for MNA and AMA. These data points were subsequently utilized in Bayesian optimization and kinetic modeling studies to optimize the reaction system.

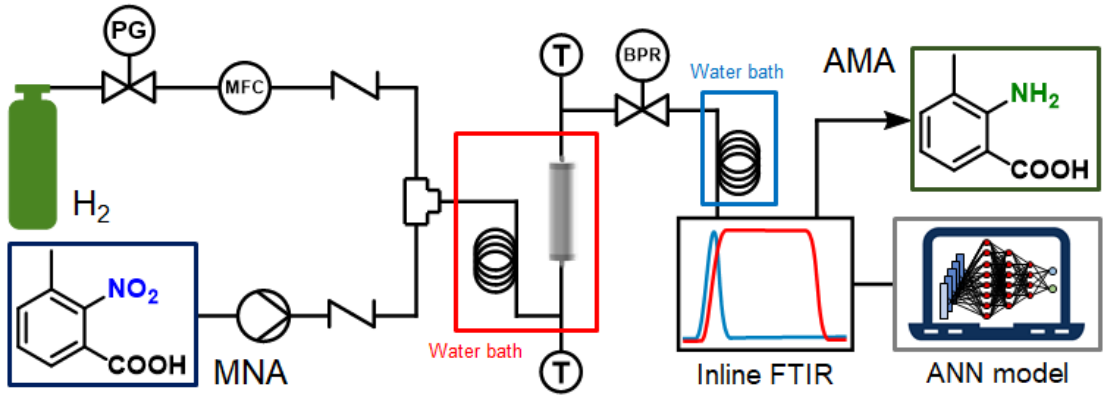

Figure 1. Heterogeneous continuous flow hydrogenation of MNA and its inline analysis

MOBO for reaction optimization.

MOBO was applied to optimize four key reaction parameters (Figure 2): reaction temperature (T_{bath}), hydrogen pressure ($P_{\mathrm{H_2}}$), initial MNA concentration (C^0_{MNA}), and MNA solution flow rate (F_{MNA}), to maximize yield and productivity. Initially, Latin Hypercube Sampling (LHS) was used to create four sets of experimental conditions, and the outcomes of these experiments formed the initial training data for a Gaussian Process (GP) surrogate model. Utilizing this GP model, the acquisition function known as qNEHVI [43] then recommended a new set of experimental conditions. With each new experiment conducted, the GP model was updated with the results, and qNEHVI continued to make further recommendations. This process was repeated iteratively until the desired levels of yield and productivity were reached. Ultimately, this method led to the identification of the optimal experimental parameters located on the Pareto Front, achieving a balance between yield and productivity.

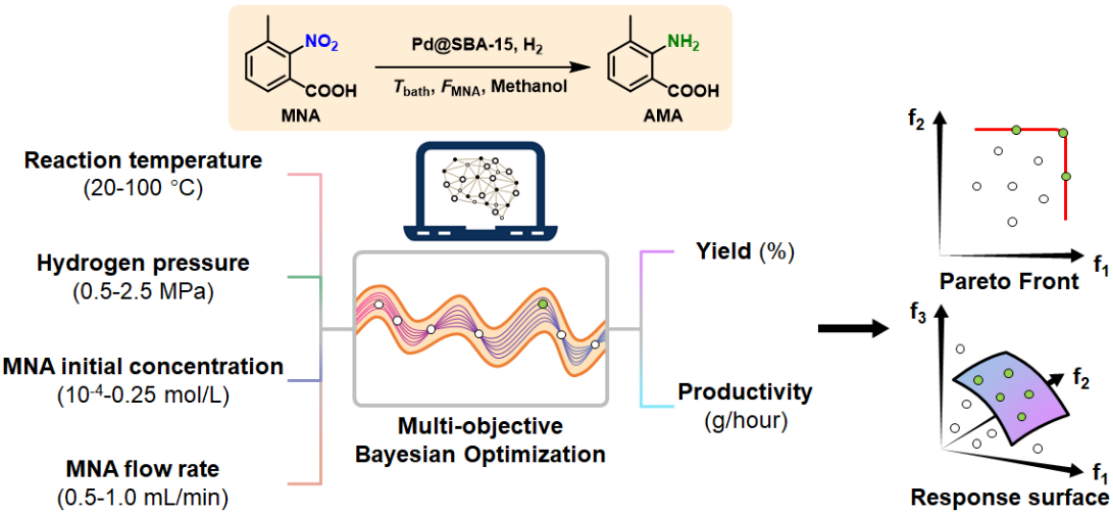

Figure 2. The MOBO of the continuous flow hydrogenation of MNA

The parameter space for the reaction was initially delineated in Figure 2. To ensure experimental safety, the hydrogen pressure and reaction temperature were capped at 2.5 MPa and 100 ˚C, respectively. The solubility of MNA in methanol dictated its concentration limit, setting the upper boundary at 0.25 mL/min. The residence time, crucial for reaction completion, was adjusted by modulating the solution's flow rate.

An excessively high flow rate could result in undue pressure build-up within the reactor tubes, while a markedly low flow rate might increase the gas phase's proportion, complicating the monitoring of MNA concentration. Consequently, the flow rate was confined to 0.5-1.0 mL/min to balance these factors.

The MOBO results are presented in Figure 3, with Figure 3a highlighting the evolution of the Pareto Front. Initial data points, marked by black crosses, were derived from LHS. The colored dots, varying in color based on iteration count, represent the data points suggested by the acquisition function. Through operation iterations with the GP model and the qNEHVI function, the data converged to form a compact Pareto Front. The data points in the upper right corner indicate the best balance between yield and productivity, showing nearly 99% yield and 0.64 g/hour productivity. The conclusive set of experimental parameters and results, which includes three sets capable of attaining these optimal levels, is detailed in Table S2.

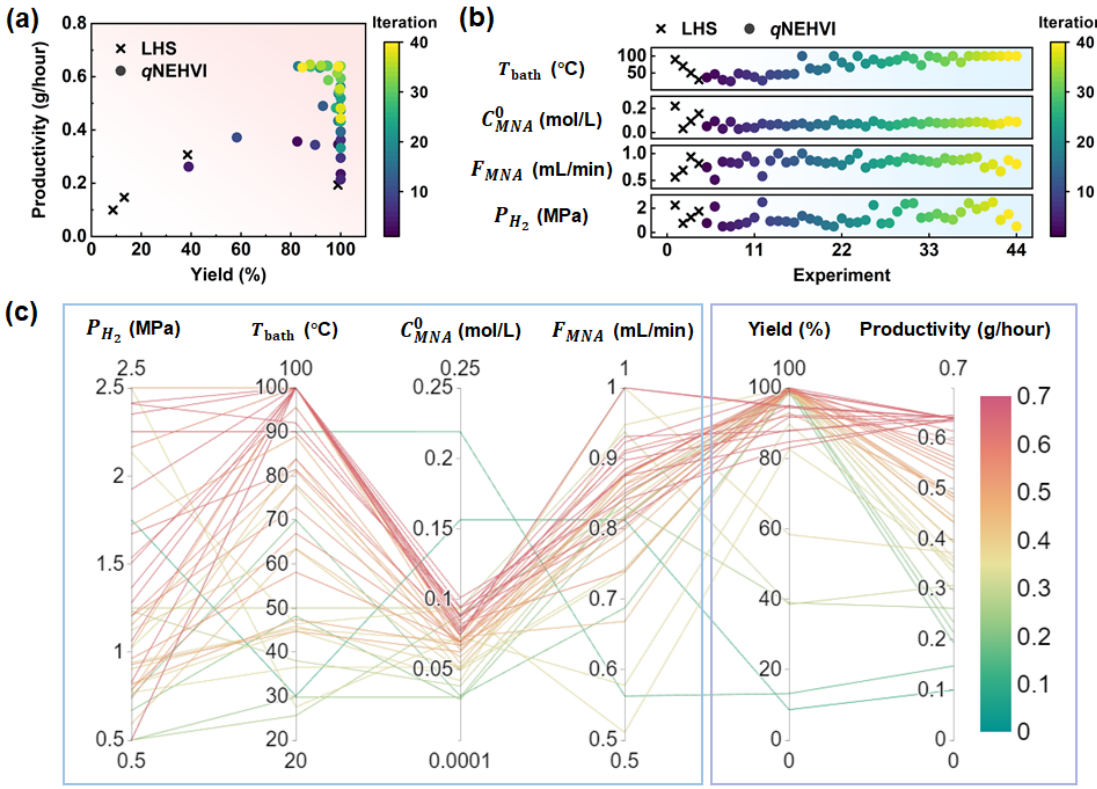

Figure 3. Results of the MOBO campaign. (a) The Pareto Front of the yield and productivity. (b) Optimization progress: each parameter *versus* experiment number. (c) Parallel coordinate plot showing the interactions between experimental parameters and results.

Figure 3b demonstrates the evolution of four optimization parameters—reaction temperature, concentration, flow rate, and hydrogen pressure—throughout the optimization process. It is observed that the reaction temperature, concentration, and flow rate values gradually stabilize, indicating that the MOBO successfully identified their optimal levels. In contrast, hydrogen pressure displayed continuous fluctuations, implying uncertainty regarding its impact on the optimization goals.

Further insights are provided by a parallel coordinate plot (Figure 3c), which delineates the preferred reaction parameter values as determined by MOBO for enhancing both yield and productivity. Notably, optimal reaction temperatures are concentrated around the upper boundary of 100 ˚C, suggesting a preference for higher temperatures to maximize yield and productivity while minimizing by-product formation. This observation highlights the advantage of multi-objective optimization, demonstrating that a 99% yield is attainable at various temperatures when yield is the sole consideration. Moreover, the plot shows that the optimal concentration and flow rate settle at approximately 0.08 mol/L and 0.86 mL/min, respectively, with neither parameter reaching its maximum or minimum limit. The analysis also indicates that hydrogen pressure does not significantly influence the optimization objectives, hinting that even the minimum hydrogen pressure level might suffice for the reaction.

For the later comparison with kinetic modeling which uses the response surface method for optimization, we performed another round of MOBO to fully explore the response surface surrounding the optimal points, with the three sets of optimal experimental parameters obtained in the previous round as the initial training set. The reaction temperature and hydrogen pressure were fixed at 100 ˚C and 0.5 MPa, respectively, acknowledging the positive correlation of high temperature and the optimization objectives and the negligible impact of hydrogen pressure. The exploration ranges for concentration and flow rate were narrowed to 0.0770-0.0884 mol/L and 0.8036-0.9227 mL/min, aiming for a thorough investigation of this refined reaction space. After 10

iterations, the results (Table S3) show that an additional four sets of experimental parameters are able to achieve the same optimal yield and productivity as the original three sets. Mapping these seven optimal sets of experimental data onto the reaction space form a response surface with an irregular shape (Figure 4).

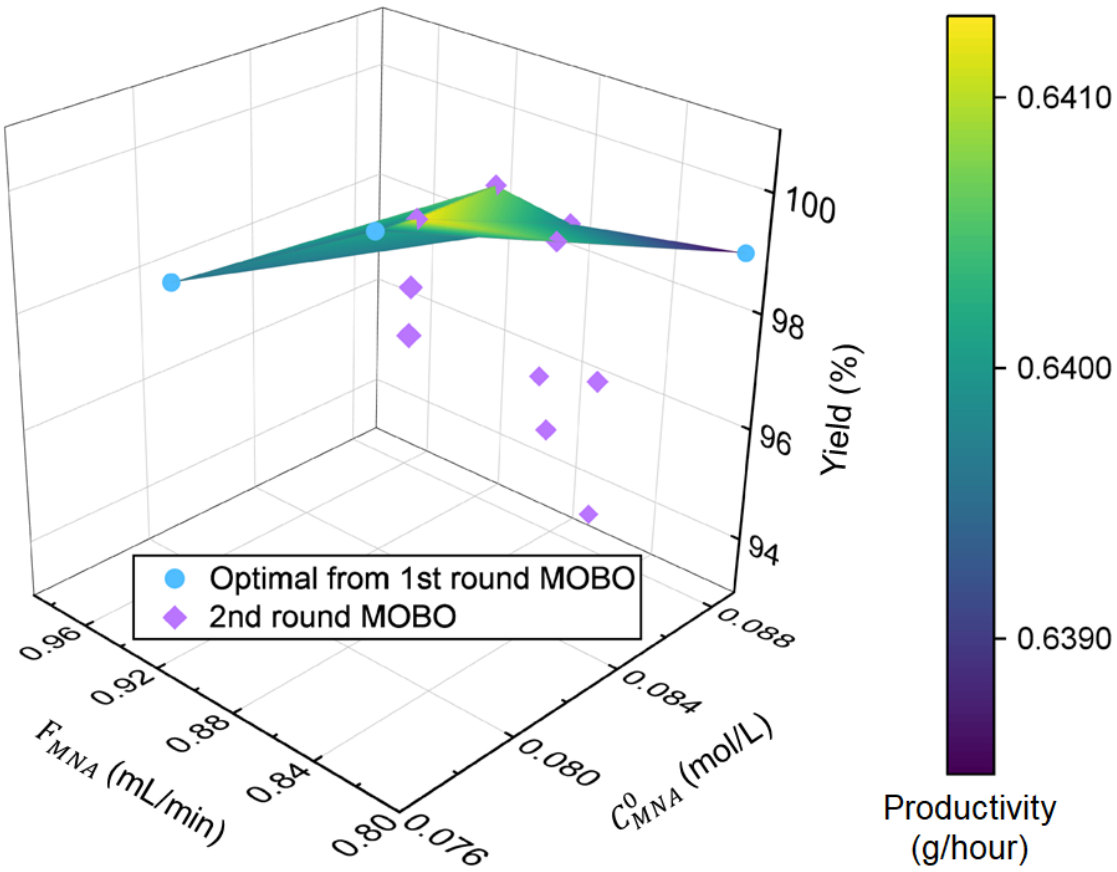

Figure 4. 3D response surface of objective values formed through fitting the optimal experimental data underwent two rounds of MOBO. The blue points represent the three optimal data points from the first round, which were used as the initial training set for the second round. The purple points indicate all the data points gathered during the second round.

Kinetic modeling for reaction optimization.

Concurrently, kinetic modeling was conducted in alignment with our previously established intrinsic kinetic modeling methodology[18]. It is important to note that non-chemical kinetic phenomena, such as gas-liquid interfacial area, fluid kinetics, solute diffusion, and mass transfer limitations, can significantly impact the accuracy of intrinsic kinetic modeling.[18] A comprehensive examination of reaction parameters (e.g., gas-to-liquid flow ratio, mean residence time) was performed to minimize these

effects, ensuring that the reaction rate data were obtained under conditions of kinetic control (see **Supporting Information**). Subsequently, experimental data were collected on the flow synthesis of AMA across various temperatures and mean residence times. This data formed the basis for our kinetic modeling efforts, during which the parameters across all models were estimated using the gPROMS (PSE, UK) parameter estimation tool [44]. Upon identifying the optimal model, a detailed examination of the reaction mechanism and the scope of this optimization approach was conducted (Figure 5).

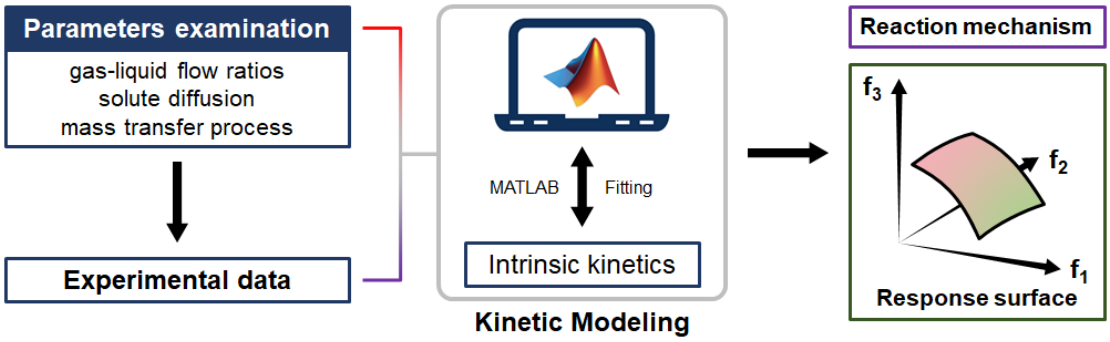

Figure 5. The overall approach for the kinetic modeling

The Langmuir-Hinshelwood-Hougen-Watson (LHHW) methodology is widely recognized for its efficacy in the kinetic modeling of heterogeneous catalytic hydrogenation processes.[44] This approach distinctively elucidates the adsorption and dissociation stages inherent in catalytic hydrogenation, thereby aiding in the accurate derivation of the reaction mechanism. The LHHW framework is structured around three pivotal stages: the Langmuir adsorption of reactants onto the catalyst surface, the surface reaction involving the adsorbed intermediates, and the subsequent desorption of the products. Typically, the surface reaction step acts as the rate-determining phase. Based on the variations in adsorption and dissociation behaviors of the reactants, four LHHW models, each characterized by unique rate expressions (r_{MNA}), have been formulated (Table 1).

Table 1. The LHHW kinetic models I-IV for MNA hydrogenation

Model[a,b]	Description	Initial rate expression
I	competitive adsorption dissociative adsorbed H_2	$r_{MNA} = \frac{-k_1 K_{H_2} K_{MNA} C_{MNA}}{\{1 + \sqrt{K_{H_2} P_{H_2}} + K_{MNA} C_{MNA} + K_{AMA} C_{AMA}\}^3}$
II	competitive adsorption nondissociative adsorbed H_2	$r_{MNA} = \frac{-k_1 K_{H_2} K_{MNA} C_{MNA} P_{H_2}}{\{1 + K_{H_2} P_{H_2} + K_{MNA} C_{MNA} + K_{AMA} C_{AMA}\}^2}$
III	noncompetitive adsorption dissociative adsorbed H_2	$r_{MNA} = \frac{-k_1 K_{H_2} K_{MNA} C_{MNA} P_{H_2}}{\{1 + K_{MNA} C_{MNA} + K_{AMA} C_{AMA}\}\{1 + \sqrt{K_{H_2} P_{H_2}}\}^2}$
IV	noncompetitive adsorption nondissociative adsorbed H_2	$r_{MNA} = \frac{-k_1 K_{H_2} K_{MNA} C_{MNA} P_{H_2}}{\{1 + K_{MNA} C_{MNA} + K_{AMA} C_{AMA}\}\{1 + K_{H_2} P_{H_2}\}}$

[a] k_1 is the reaction rate constant of r_{MNA}; K_{H_2}, K_{MNA}, and K_{AMA} are adsorption equilibrium constants of H_2, MNA, and AMA, respectively; C_{MNA} and C_{AMA} are the concentration of MNA and AMA in the collected solution, respectively; P_{H_2} is the pressure of H_2. [b] Experimental conditions for data collection: C^0_{MNA} (0.1 mol/L), F_{MNA} (0.5 mL/min), F_{H_2} (20 mL/min), P_{H_2} (0.5 MPa).

The experimental data obtained were subsequently employed to fit these LHHW rate expressions as objective functions in MATLAB, achieved through the fmincon function with a Sequential Quadratic Programming (SQP) method. The ordinary differential equations (ODEs) were solved using the ODE45 function. We fitted the kinetic models to the experimental data obtained at the reaction temperatures of 30 ˚C (303.15 K), 40 ˚C (313.15 K), 50 ˚C (323.15 K), and 60 ˚C (333.15 K), with the results of these fittings shown in Figure 6 and Figure S3.

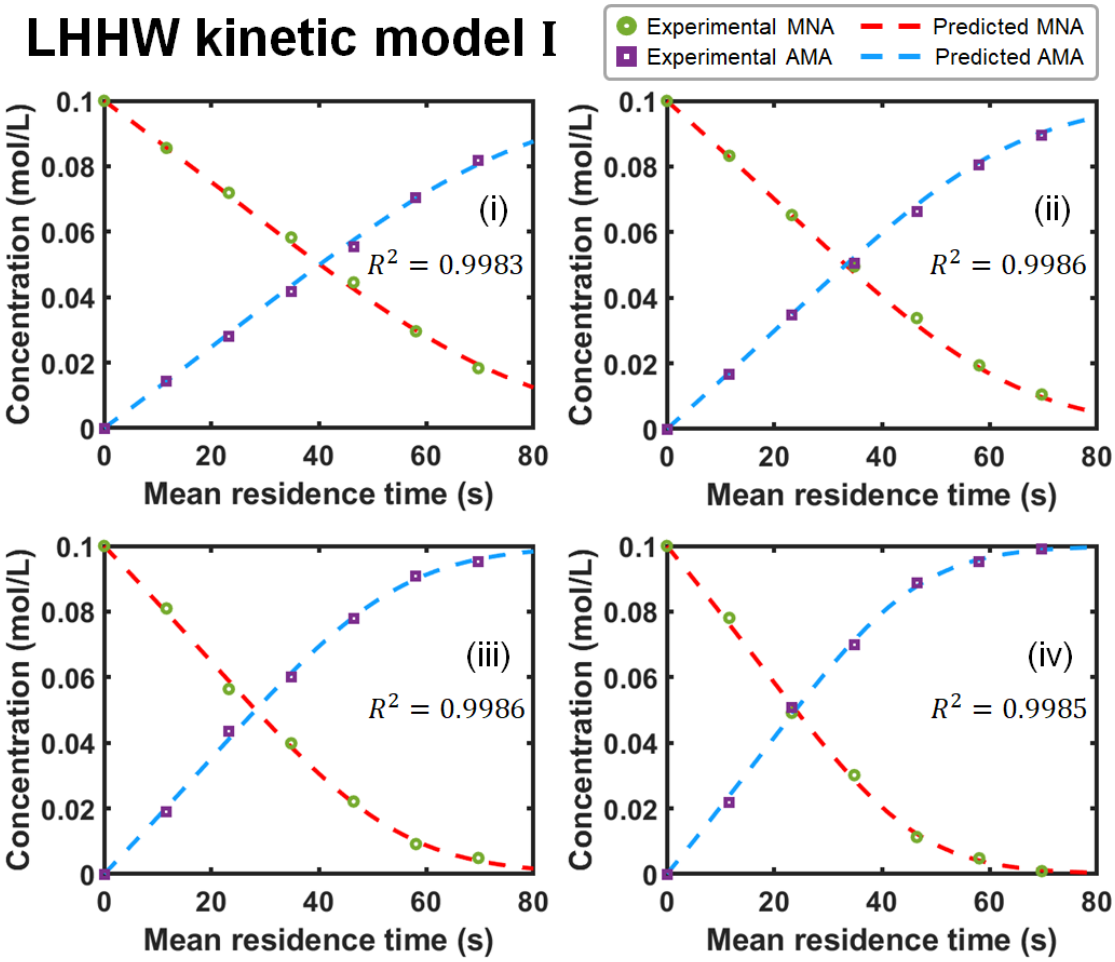

Figure 6. Fitted curves of the LHHW kinetic model I: (i) 30 ˚C, (ii) 40 ˚C, (iii) 50 ˚C, and (iv) 60 ˚C.

Each LHHW kinetic model was evaluated by estimating model parameters using the gPROMS parameter estimation tool. Based on these estimated parameters, various statistical indicators were calculated to assess the fitting performance of each model (see **Supporting Information**). The selection criteria for the optimal model included the highest value of regression coefficient (R^2) alongside the lowest sum of squared residuals (SSR) and mean relative error (MRE). Upon comparison of these indicators in Table 2, the LHHW kinetic model I emerged as the most fitting according to these criteria, thereby establishing it as the optimal kinetic model. Furthermore, the chosen LHHW kinetic model I was further evaluated by comparing the experimental reaction rates with those predicted by the model in Figure 7a. This alignment between experimental and predicted rates underscores the robustness of the LHHW kinetic model I in simulating the reaction kinetics under study.

Table 2. Statistical evaluations related to experimental and predicted concentrations of MNA for different LHHW kinetic models

Model	Stat. param.	30 ˚C	40 ˚C	50 ˚C	60 ˚C
I	R^2	0.9983	0.9986	0.9986	0.9985
	SSR × 10^5	0.874	0.953	1.07	1.29
	MRE (%)	2.23	3.20	5.51	10.2
II	R^2	0.9964	0.9984	0.9979	0.9983
	SSR × 10^5	1.90	1.07	1.67	1.54
	MRE (%)	4.32	4.86	6.25	11.9
III	R^2	0.9967	0.9982	0.9983	0.9979
	SSR × 10^5	1.72	1.18	1.32	1.89
	MRE (%)	3.95	4.94	7.71	12.4
IV	R^2	0.9969	0.9982	0.9978	0.9979
	SSR × 10^5	1.64	1.19	1.72	1.88
	MRE (%)	3.80	4.28	8.19	12.7

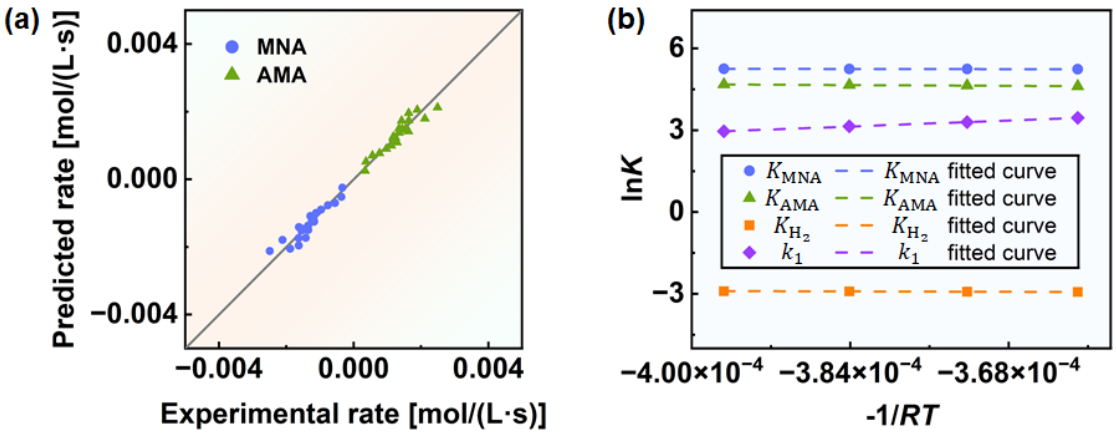

Figure 7. (a) Comparison of experimental reaction rate and predicted reaction rate using the LHHW kinetic model I. (b) Fitted curves of Arrhenius equation for LHHW model I.

The kinetic and thermodynamic parameters of the LHHW model I are determined and shown in Table 3. The k_1, K_{H_2}, K_{MNA}, and K_{AMA} were obtained through kinetic model fitting in MATLAB. The activation energy (E) and the pre-exponential factor (k_0) were obtained from the Arrhenius equation (Equation 6) and its variant (Equation

7) for the surface reaction:

$$k = k_0 e^{-\frac{E}{RT}} \quad (6)$$

$$\ln k = -\frac{E}{RT} + \ln k_0 \quad (7)$$

where k is the reaction rate constant; k_0 is the pre-exponential factor; E is the activation energy; R is the universal gas constant; T the temperature in K.

Table 3. Various kinetic and thermodynamic parameters of the LHHW model I

Para.	Temperature (K)				Thermodynamic parameters	
	303.15	313.15	323.15	333.15	E (kJ mol^{-1})	k_0 (mol L^{-1} s^{-1})
k_1 (mol L^{-1} s^{-1})	19.290	23.072	26.972	31.590	13.740	4.503×10^3
Para.	Temperature (K)				Thermodynamic parameters	
	303.15	313.15	323.15	333.15	E_a (kJ mol^{-1})	K_0
K_{MNA} (L mol^{-1})	190.988	189.882	188.768	187.866	-0.465	158.823 (L mol^{-1})
K_{AMA} (L mol^{-1})	107.645	105.101	102.990	100.703	-1.849	51.685 (L mol^{-1})
K_{H_2} (MPa^{-1})	0.0548	0.0543	0.0538	0.0533	-0.776	0.0403 (MPa^{-1})

The activation energy of the surface reaction is 13.740 kJ/mol through the linear fitting method, and the adsorption heats (E_a) of H_2, MNA, and AMA are all negative, signifying that the adsorption process is exothermic (Figure 7b). The adsorption heat (E_a) and the pre-exponential factor (K_0) were also estimated using the Arrhenius equation (Equation 8) for the adsorption process:

$$\ln K = -\frac{E_a}{RT} + \ln K_0 \quad (8)$$

where K is the adsorption equilibrium constant; K_0 is the pre-exponential factor; E_a is the adsorption heat; R is the universal gas constant; T the temperature in K.

To achieve reaction optimization via intrinsic kinetic modeling, response surfaces of the kinetic model were generated across various MNA concentrations, with yield represented on the Z axis and the productivity illustrated through a color map (Figure

8). While it is feasible to attain a yield nearing 99% at a lower concentration and reduced mean residence time, optimizing both productivity and yield simultaneously—targeting the yellow area in Figure 8—requires an increase in both the mean residence time and MNA concentration. Under these optimized conditions, it is possible to achieve both a yield and productivity of up to 99% and 1.13 g/hour, respectively. The results predicted by the kinetic model at the optimized conditions were all confirmed by experimental results (Table S4).

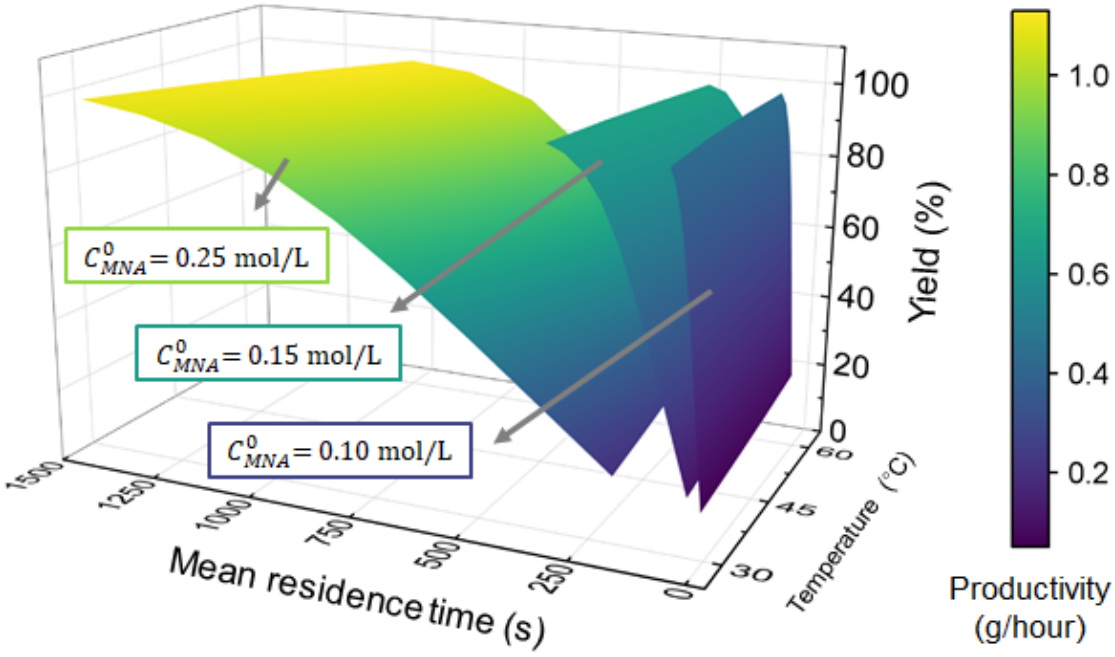

Figure 8. 3D response surface of objective values formed through the LHHW kinetic model I

Comparison of MOBO and kinetic modeling.

Table 4 presents the optimal reaction parameters and results from the two optimization approaches. The MOBO achieved an optimal yield of approximately 99% and productivity of 0.64 g/hour, respectively. Conversely, kinetic modeling achieved a similar optimal yield (~99%) but attained higher productivity (1.13 g/hour). The variation in optimal productivity was attributed to the distinct strategies for manipulating the residence time of the two approaches. MOBO modulated the residence time by adjusting the solution's flow rate, keeping the catalyst mass constant

within the MPBR. This approach was favored because MOBO was implemented in an automated manner, discouraging altering the catalyst quantity in the MPBR. Manually increasing the catalyst quantity could further increase productivity. Conversely, the intrinsic kinetic modeling methodology, which presumes that non-chemical kinetics phenomena (e.g., mass transfer, solute diffusion, flow dynamics) minimally impact the reaction, does not permit free variation of the flow rate but requires adjustment of the catalyst mass to maintain a constant solution flow rate.

Table 4. The optimal reaction parameters and results of MOBO and kinetic modeling

Data type[a]	C^0_{MNA} (mol/L)	F_{MNA} (mL/min)	Yield (%)	Productivity (g/hour)
MOBO	0.0770	0.9227	99.25	0.6396
	0.0805	0.8763	99.99	0.6397
	0.0884	0.8036	99.09	0.6385
	0.0854	0.8547	99.18	0.6404
	0.0868	0.8648	99.08	0.6398
	0.0846	0.8741	99.99	0.6407
	0.0817	0.8733	99.99	0.6413

Data type[b]	T_{bath} (˚C)	MRT (s)	Yield (%)	Productivity (g/hour)	Yield (%)	Productivity (g/hour)
			Predicted data		Experimental data	
Kinetic modeling	60	980	99.16	1.1242	99.98	1.1335
	55	1050	99.02	1.1226	99.92	1.1328
	50	1150	99.02	1.1226	99.95	1.1332
	45	1280	99.11	1.1237	99.93	1.1329
	40	1400	99.06	1.1231	99.91	1.1327

[a]Experimental conditions for data collection: T_{bath} (100 ˚C), P_{H_2} (0.5 MPa). [b]Experimental conditions for data collection: C^0_{MNA} (0.25 mol/L), F_{MNA} (0.5 mL/min), F_{H_2} (20 mL/min), P_{H_2} (0.5 MPa).

Regarding optimization efficiency, MOBO excels in swiftly identifying the optimal reaction space by utilizing the Pareto Front. With an additional round of optimization, it effectively narrowed down the search to the seven promising parameter combinations (Figure 4). These selected points are subsequently used to construct the response surface for the optimization objectives, effectively mapping out the optimal reaction space from a broader set of possibilities. The integration of inline FTIR with MOBO enhances its capability to optimize reactions rapidly and with high precision. In contrast,

kinetic modeling requires significant time and resources. The process involves the collection of large amounts of experimental data, the fitting of kinetic equations, and the derivation of scientific models. This approach is more labor intensive and slower than the simplified and data-saving process of MOBO.

Although kinetic modeling is may not be as efficient as MOBO for reaction optimization, it offers a distinct advantage in terms of understanding reaction kinetics. While Bayesian Optimization is engineered for rapid convergence to optimal solutions, it lacks the capability to generate a comprehensive response surface across the full reaction space (Figure 4). In contrast, kinetic modeling allows for the calculation of a spectrum of optimal reaction parameters by leveraging predictions from scientific models. The response surfaces derived from kinetic modeling (Figure 8) provide valuable insights into reaction optimization by offering a visual representation of the entire reaction space, thereby highlighting trends and delineating the boundaries of optimization possibilities [7, 45].

Conclusions

In this work, we developed a heterogeneous continuous flow hydrogenation system enhanced with real-time inline infrared monitoring utilizing an ANN model for optimizing the synthesis of the crucial pesticide intermediate, AMA. This work systematically undertook and compared MOBO and kinetic modeling approaches to optimize the reaction process. In only 40 iterations, MOBO efficiently identified the Pareto optimal parameter combinations within the vast and intricate reaction space. The compromise between yield and productivity was impressively achieved. Conversely, intrinsic kinetic modeling revealed the activation energy of this hydrogenation reaction and characterized the hydrogen adsorption as competitive dissociative adsorption. This approach provided a comprehensive understanding of how variations in parameters affect the reaction results. Simultaneous optimization of yield and productivity was also achieved by leveraging the response surfaces generated from the kinetic model.

While MOBO is efficient and accurate in determining the optimal reaction conditions, kinetic modeling provides insight into the mechanistic details of the reaction and offers comprehensive optimization possibilities over the entire reaction space. Thus, the in-depth study of heterogeneous continuous flow hydrogenation systems benefits from the synergistic application of MOBO and kinetic modeling. This dual approach enriches our understanding of reaction optimization and provides a deeper exploration of continuous-flow hydrogenation systems, offering valuable prospects for future research and development in this field.

Declaration of Competing Interest

The authors declare that they have no known competing financial interests or personal relationships that could have appeared to influence the work reported in this paper.

Acknowledgments

This research was supported by the Joint Funds of the Zhejiang Provincial Natural Science Foundation of China under Grant No. LHDMZ23B060001，Zhejiang Province Science and Technology Plan Project under Grant No. 2022C01179, and the National Natural Science Foundation of China under Grant No. 22108252).

Appendix A. Supplementary data

Supplementary data to this article can be found online at XXXXXXXXXXXXXXX.

References

[1] R.Y. Qu, K. Junge, M. Beller, Hydrogenation of Carboxylic Acids, Esters, and Related Compounds over Heterogeneous Catalysts: A Step toward Sustainable and Carbon-Neutral Processes, Chem. Rev. 123 (3) (2023) 1103-1165, https://doi.org/10.1021/acs.chemrev.2c00550.

[2] T. Wagener, A. Heusler, Z. Nairoukh, K. Bergander, C.G. Daniliuc, F. Glorius, Accessing (Multi)Fluorinated Piperidines Using Heterogeneous Hydrogenation, ACS Catal. 10 (20) (2020) 12052-12057, https://doi.org/10.1021/acscatal.0c03278.

[3] L. Lückemeier, T. De Vos, L. Schlichter, C. Gutheil, C.G. Daniliuc, F. Glorius, Chemoselective Heterogeneous Hydrogenation of Sulfur Containing Quinolines under Mild Conditions, J. Am. Chem. Soc. (2024) Advance Article, https://doi.org/10.1021/jacs.3c11163.
[4] T. Yasukawa, R. Masuda, S. Kobayashi, Development of heterogeneous catalyst systems for the continuous synthesis of chiral amines via asymmetric hydrogenation, Nat. Catal. 2 (12) (2019) 1088-1092, https://doi.org/10.1038/s41929-019-0371-y.
[5] Y. Saito, Y. Sato, S. Kobayashi, Continuous-Flow Enantioselective Hydrogenative Enyne Cyclization with Chiral Heterogeneous Rh Catalysts, ACS Catal. 14 (4) (2024) 2202-2206, https://doi.org/10.1021/acscatal.3c05868.
[6] M. González-Esguevillas, D.F. Fernández, J.A. Rincón, M. Barberis, O. de Frutos, C. Mateos, S. García-Cerrada, J. Agejas, D.W.C. MacMillan, Rapid Optimization of Photoredox Reactions for Continuous-Flow Systems Using Microscale Batch Technology, ACS Cent. Sci. 7 (7) (2021) 1126-1134, https://doi.org/10.1021/acscentsci.1c00303.
[7] C.J. Taylor, A. Pomberger, K.C. Felton, R. Grainger, M. Barecka, T.W. Chamberlain, R.A. Bourne, C.N. Johnson, A.A. Lapkin, A Brief Introduction to Chemical Reaction Optimization, Chem. Rev. 123 (6) (2023) 3089-3126, https://doi.org/10.1021/acs.chemrev.2c00798.
[8] D. Lendrem, M. Owen, S. Godbert, DOE (design of experiments) in development chemistry: Potential obstacles, Org. Process Res. Dev. 5 (3) (2001) 324-327, https://doi.org/10.1021/op000025i.
[9] M. Strohmann, A. Bordet, A.J. Vorholt, W. Leitner, Tailor-made biofuel 2-butyltetrahydrofuran from the continuous flow hydrogenation and deoxygenation of furfuralacetone, Green Chem. 21 (23) (2019) 6299-6306, https://doi.org/10.1039/c9gc02555c.
[10] Y.T. Wang, P. Prinsen, K.S. Triantafyllidis, S.A. Karakoulia, P.N. Trikalitis, A. Yepez, C. Len, R. Luque, Comparative Study of Supported Monometallic Catalysts in the Liquid-Phase Hydrogenation of Furfural: Batch Versus Continuous Flow, ACS Sustainable Chem. Eng. 6 (8) (2018) 9831-9844, https://doi.org/10.1021/acssuschemeng.8b00984.
[11] M. Kundra, T. Grall, D. Ng, Z.L. Xie, C.H. Hornung, Continuous Flow Hydrogenation of Flavorings and Fragrances Using 3D-Printed Catalytic Static Mixers, Ind. Eng. Chem. Res. 60 (5) (2021) 1989-2002, https://doi.org/10.1021/acs.iecr.0c05671.
[12] P.X. Wang, Z.P. Peng, X.P. Wang, Y. Lin, H.B. Hong, F. Chen, X.K. Chen, J.S. Zhang, Continuous hydrogenation of nitriles to primary amines with high selectivity in flow, Chem. Eng. Sci. 269 (2023) 118460, https://doi.org/10.1016/j.ces.2023.118460.
[13] M.D. Peris-Díaz, M.A. Sentandreu, E. Sentandreu, Multiobjective optimization of liquid chromatography-triple-quadrupole mass spectrometry analysis of underivatized human urinary amino acids through chemometrics, Anal. Bioanal. Chem. 410 (18) (2018) 4275-4284, https://doi.org/10.1007/s00216-018-1083-x.
[14] B. Zhang, A. Mathoor, T. Junkers, High Throughput Multidimensional Kinetic Screening in Continuous Flow Reactors, Angew. Chem., Int. Ed. 62 (38) (2023) e202308838, https://doi.org/10.1002/anie.202308838.
[15] P. Rojahn, K.D.P. Nigam, F. Schael, Experimental study and kinetic modeling of continuous flow conversion of fructose to 5-(chloromethyl)furfural using micro- and millistructured coiled flow inverter, Chem. Eng. J. 450 (2022) 138243, https://doi.org/10.1016/j.cej.2022.138243.
[16] Z.F. Yan, C.C. Du, Y.B. Wang, J. Deng, G.S. Luo, Dehydrochlorination of β-chlorohydrin in continuous microflow system: Reaction kinetics and process intensification, Chem. Eng. J. 444 (2022) 136498, https://doi.org/10.1016/j.cej.2022.136498.

[17] X.Y. Lin, K. Wang, B.Y. Zhou, G.S. Luo, A microreactor-based research for the kinetics of polyvinyl butyral (PVB) synthesis reaction, Chem. Eng. J. 383 (2020) 123181, https://doi.org/10.1016/j.cej.2019.123181.
[18] H.T. Xue, T.T. Qi, W.K. Su, K.J. Wu, A. Su, Heterogeneous Continuous Flow Hydrogenation of Hexafluoroacetone Trihydrate and Its Kinetic Modeling, Ind. Eng. Chem. Res. 62 (15) (2023) 6121-6129, https://doi.org/10.1021/acs.iecr.3c00291.
[19] Z.Q. Yu, M.N. Ren, P. Li, J.D. Zhou, N. Li, X. Li, H.C. Fan, Continuous hydrogenation of 2-(4-nitrophenyl) butanoic acid: Kinetics study in a micropacked-bed reactor, Chem. Eng. Sci. 271 (2023) 118565, https://doi.org/10.1016/j.ces.2023.118565.
[20] N.K. Razdan, T.C. Lin, A. Bhan, Concepts Relevant for the Kinetic Analysis of Reversible Reaction Systems, Chem. Rev. 123 (6) (2023) 2950-3006, https://doi.org/10.1021/acs.chemrev.2c00510.
[21] T. Dahou, F. Defoort, B. Khiari, M. Labaki, C. Dupont, M. Jeguirim, Role of inorganics on the biomass char gasification reactivity: A review involving reaction mechanisms and kinetics models, Renewable Sustainable Energy Rev. 135 (2021) 110136, https://doi.org/10.1016/j.rser.2020.110136.
[22] Z.H. Yu, N. Ji, X.Y. Li, R. Zhang, Y.A. Qiao, J. Xiong, J. Liu, X.B. Lu, Kinetics Driven by Hollow Nanoreactors: An Opportunity for Controllable Catalysis, Angew. Chem., Int. Ed. 62 (3) (2023) e202213612, https://doi.org/10.1002/anie.202213612.
[23] C. Wang, Y. Yang, Z.L. Huang, J.Y. Sun, J.D. Wang, Y.R. Yang, B. Du, Gas-liquid mass transfer in a gas-liquid-solid three-phase moving bed, Chem. Eng. J. 420 (2021) 130449, https://doi.org/10.1016/j.cej.2021.130449.
[24] C. Wang, Y. Yang, Z.L. Huang, J.Y. Sun, Z.W. Liao, J.D. Wang, Y.R. Yang, B. Du, Flow regimes in a gas-liquid-solid three-phase moving bed, AIChE J. 67 (11) (2021) e17374, https://doi.org/10.1002/aic.17374.
[25] A.M.K. Nambiar, C.P. Breen, T. Hart, T. Kulesza, T.F. Jamison, K.F. Jensen, Bayesian Optimization of Computer-Proposed Multistep Synthetic Routes on an Automated Robotic Flow Platform, ACS Cent. Sci. 8 (6) (2022) 825-836, https://doi.org/10.1021/acscentsci.2c00207.
[26] J.H. Dunlap, J.G. Ethier, A.A. Putnam-Neeb, S. Iyer, S.X.L. Luo, H.S. Feng, J.A.G. Torres, A.G. Doyle, T.M. Swager, R.A. Vaia, P. Mirau, C.A. Crouse, L.A. Baldwin, Continuous flow synthesis of pyridinium salts accelerated by multi-objective Bayesian optimization with active learning, Chem. Sci. 14 (30) (2023) 8061-8069, https://doi.org/10.1039/d3sc01303k.
[27] O.J. Kershaw, A.D. Clayton, J.A. Manson, A. Barthelme, J. Pavey, P. Peach, J. Mustakis, R.M. Howard, T.W. Chamberlain, N.J. Warren, R.A. Bourne, Machine learning directed multi-objective optimization of mixed variable chemical systems, Chem. Eng. J. 451 (2023) 138443, https://doi.org/10.1016/j.cej.2022.138443.
[28] A.M. Schweidtmann, A.D. Clayton, N. Holmes, E. Bradford, R.A. Bourne, A.A. Lapkin, Machine learning meets continuous flow chemistry: Automated optimization towards the Pareto front of multiple objectives, Chem. Eng. J. 352 (2018) 277-282, https://doi.org/10.1016/j.cej.2018.07.031.
[29] A.D. Clayton, E.O. Pyzer-Knapp, M. Purdie, M.F. Jones, A. Barthelme, J. Pavey, N. Kapur, T.W. Chamberlain, A.J. Blacker, R.A. Bourne, Bayesian Self-Optimization for Telescoped Continuous Flow Synthesis, Angew. Chem., Int. Ed. 62 (3) (2023) e202214511, https://doi.org/10.1002/anie.202214511.
[30] C.J. Taylor, K.C. Felton, D. Wigh, M.I. Jeraal, R. Grainger, G. Chessari, C.N. Johnson, A.A. Lapkin, Accelerated Chemical Reaction Optimization Using Multi-Task Learning, ACS Cent. Sci. 9 (5) (2023) 957-968, https://doi.org/10.1021/acscentsci.3c00050.
[31] P.W. Liu, H. Jin, Y. Chen, D.R. Wang, H.H. Yan, M.Z. Wu, F. Zhao, W.P. Zhu, Process analytical

technologies and self-optimization algorithms in automated pharmaceutical continuous manufacturing, Chin. Chem. Lett. 35 (3) (2024) 108877, https://doi.org/10.1016/j.cclet.2023.108877.
[32] J. Britton, S. Majumdar, G.A. Weiss, Continuous flow biocatalysis, Chem. Soc. Rev. 47 (15) (2018) 5891-5918, https://doi.org/10.1039/c7cs00906b.
[33] P. Sagmeister, R. Lebl, I. Castillo, J. Rehrl, J. Kruisz, M. Sipek, M. Horn, S. Sacher, D. Cantillo, J.D. Williams, C.O. Kappe, Advanced Real-Time Process Analytics for Multistep Synthesis in Continuous Flow, Angew. Chem., Int. Ed. 60 (15) (2021) 8139-8148, https://doi.org/10.1002/anie.202016007.
[34] P. Sagmeister, R. Hierzegger, J.D. Williams, C.O. Kappe, S. Kowarik, Artificial neural networks and data fusion enable concentration predictions for inline process analytics, Digital Discovery 1 (2022) 405-412, https://doi.org/10.1039/D2DD00006G.
[35] K.J. Chai, R.Q. Shen, T.T. Qi, J.L. Chen, W.K. Su, A. Su, Continuous-Flow Hydrogenation of Nitroaromatics in Microreactor with Mesoporous Pd@SBA-15, Processes 11 (4) (2023) 1074, https://doi.org/10.3390/pr11041074.
[36] R.Z. Liang, X.N. Duan, J.S. Zhang, Z.H. Yuan, Bayesian based reaction optimization for complex continuous gas-liquid-solid reactions, React. Chem. Eng. 7 (3) (2022) 590-598, https://doi.org/10.1039/d1re00397f.
[37] E. Braconi, E. Godineau, Bayesian Optimization as a Sustainable Strategy for Early-Stage Process Development? A Case Study of Cu-Catalyzed C-N Coupling of Sterically Hindered Pyrazines, ACS Sustainable Chem. Eng. 11 (28) (2023) 10545-10554, https://doi.org/10.1021/acssuschemeng.3c02455.
[38] A. Navid, S. Khalilarya, M. Abbasi, Diesel engine optimization with multi-objective performance characteristics by non-evolutionary Nelder-Mead algorithm: Sobol sequence and Latin hypercube sampling methods comparison in DoE process, Fuel 228 (2018) 349-367, https://doi.org/10.1016/j.fuel.2018.04.142.
[39] T.T. Qi, G.H. Luo, H.T. Xue, F. Su, J.L. Chen, W.K. Su, K.J. Wu, A. Su, Continuous heterogeneous synthesis of hexafluoroacetone and its machine learning-assisted optimization, J. Flow Chem. 13 (3) (2023) 337-346, https://doi.org/10.1007/s41981-023-00273-1.
[40] N. Leonenko, A. Malyarenko, Matérn Class Tensor-Valued Random Fields and Beyond, J. Stat. Phys. 168 (6) (2017) 1276-1301, https://doi.org/10.1007/s10955-017-1847-2.
[41] J.Y.Z. Zhang, N. Sugisawa, K.C. Felton, S. Fuse, A.A. Lapkin, Multi-objective Bayesian optimisation using *q*-noisy expected hypervolume improvement (*q*NEHVI) for the Schotten-Baumann reaction, React. Chem. Eng. (2024) Advance Article, https://doi.org/10.1039/d3re00502j.
[42] G.H. Luo, X.L. Yang, W.K. Su, T.T. Qi, Q.L. Xu, A. Su, Optimizing telescoped heterogeneous catalysis with noise-resilient multi-objective Bayesian optimization, ChemRxiv (2024) Advance Article, https://doi.org/10.26434/chemrxiv-2024-9257k.
[43] S. Daulton, M. Balandat, E. Bakshy, Parallel Bayesian Optimization of Multiple Noisy Objectives with Expected Hypervolume Improvement, Advances in Neural Information Processing Systems 34 (2021) 2187-2200.
[44] B.R. Patil, A.H. Bari, D.V. Pinjari, A.B. Pandit, Intrinsic Kinetics of Three-Phase Slurry Hydrogenation of *o*-Nitrocardanol to *o*-Aminocardanol over Raney Nickel Catalyst, Ind. Eng. Chem. Res. 56 (39) (2017) 11034-11041, https://doi.org/10.1021/acs.iecr.7b02523.
[45] F. Wagner, P. Sagmeister, C.E. Jusner, T.G. Tampone, V. Manee, F.G. Buono, J.D. Williams, C.O. Kappe, A Slug Flow Platform with Multiple Process Analytics Facilitates Flexible Reaction Optimization, Adv. Sci. (2024) 2308034, https://doi.org/10.1002/advs.202308034.